Seasonal effect on hemispheric asymmetry in ionospheric horizontal and field-aligned currents

A. B. Workayehu, H. Vanhamäki, and A. T. Aikio

Ionospheric Physics Research Unit, University of Oulu, Finland.

Key Points:

- Hemispheric asymmetry in auroral currents is largest during winter and autumn, and smallest during summer and spring
- Low Kp conditions show the strongest asymmetry in winter, with maximum NH/SH ratio of 1.21 for FAC and 1.10 for DF-current
- Currents in the evening sector contribute more to the high NH/SH ratio than the morning sector

Corresponding author: A. B. Workayehu, abiyot.workayehu@oulu.fi

Abstract

We present a statistical investigation of the seasonal effect on hemispheric asymmetry in the auroral currents during low (Kp $<$ 2) and high (Kp $\geq$ 2) geomagnetic activity. Five years of magnetic data from the Swarm satellites has been analysed by applying the spherical elementary current system (SECS) method. Bootstrap resampling has been used to remove the seasonal differences between the hemispheres in the dataset. In general, the currents are larger in the Northern Hemisphere (NH) than in the Southern Hemisphere (SH). Asymmetry is larger during low than high Kp, and during winter and autumn than summer and spring. The NH/SH ratio for FACs in winter, autumn, spring and summer are 1.17 $\pm$ 0.05, 1.14 $\pm$ 0.05, 1.07 $\pm$ 0.04 and 1.02 $\pm$ 0.04, respectively. The largest asymmetry is observed during low Kp winter, when the excess in the NH currents is 21$\pm$5% in FAC, 14 $\pm$ 3% in curl-free (CF), and 10$\pm$3% in divergence-free (DF) current. We also find that evening sector (13-24 MLT) contributes more to the high NH/SH ratio than the morning (01-12 MLT) sector. The physical mechanisms producing the hemispheric asymmetry are not presently understood. We calculated the background ionospheric conductances during low Kp conditions from the IRI, NRLMSISE and CHAOS models. The results indicate that only a small part of the hemispheric asymmetry can be explained by variations in the solar induced conductances.

1 Introduction

Several previous observational and model-based studies have investigated the effects of seasons on the auroral current systems (e.g., Fujii et al., 1981; Papitashvili et al., 2002; Christiansen et al., 2002; Juusola et al., 2009; Green et al., 2009; Huang et al., 2017, and references therein). With the auroral current systems, we refer to both the field aligned current (FAC) and ionospheric horizontal currents. The horizontal part of the auroral current system can further be divided into Pedersen and Hall currents which can in many situtations be approximated by the curl-free (CF) and divergence-free (DF) horizontal current components, respectively.

From TRIAD satellite data in the Northern Hemisphere (NH), Fujii et al. (1981) found the seasonal effect to be confined mainly on the dayside and the intensity of FAC amplitude in summer to be about twice as large as in winter. From model calculation, Papitashvili et al. (2002) found 1.35 times stronger FAC in the local summer than the winter season. From Ørsted satellite magnetic field measurements for the northern winter and southern summer seasons, Christiansen et al. (2002) calculated the southern summer to northern winter ratio of FAC during quiet and disturbed conditions to be 1.5 and 1.8, respectively. Juusola et al. (2009) using CHAMP data and Green et al. (2009) using Iridium constellation found 1.4 and 1.3 times stronger FAC in the summer than the winter season, respectively. From Swarm magnetic measurements, Huang et al. (2017) reported about 1.5 times stronger eastward electrojet in local summer than in winter, while the westward electrojet was less dependent on seasons. In summary, the summer to winter ratio in auroral currents has been reported to be from 1.35 to 2. Much of the seasonal variations are attributed to the solar extreme ultraviolet (EUV) radiation contribution to the ionospheric conductivity.

Hemispheric asymmetry in currents at high latitudes has been reported in several previous studies (Green et al., 2009; Coxon et al., 2016; Laundal et al., 2016; Milan et al., 2017; Huang et al., 2017; Workayehu et al., 2019). Green et al. (2009) found larger average currents in the NH than SH using the cross-track component of magnetic field data measured by Iridium satellites. However, the authors concluded that the difference can be explained in terms of the Iridium orbit configuration. Coxon et al. (2016) and Milan et al. (2017) using the Active Magnetosphere and Planetary Electrodynamics Response Experiment (AMPERE) data showed that averaged over several years, currents in the NH were clearly larger than in the SH. Coxon et al. (2016) suggested that the NH

may react more strongly to dayside reconnection than the SH, while Milan et al. (2017) stated that it is not clear if this difference is instrumental or real. Laundal et al. (2017) raised the question of the role of data analysis method with respect to this result, and suggest further studies. Huang et al. (2017) studied the seasonal and Interplanetary Magnetic Field (IMF) dependence of FAC and Hall currents within the auroral ionosphere using Swarm magnetometer data. They found larger auroral electrojets in the NH than in the SH during local summer seasons.

Recently Workayehu et al. (2019), here after referred to as Paper 1, presented statistical distributions of the auroral current systems, FACs as well as the horizontal curl-free (CF) and divergence-free (DF) currents, both in the NH and SH during low ($Kp < 2$) and high ($Kp \geq 2$) geomagnetic activity conditions by using Swarm satellite data. We examined Hemispheric differences of auroral currents averaged over all local seasons in terms of the north to south ratios of integrated FACs and averaged horizontal currents. We found significant hemispheric asymmetry during low activity conditions, with about 10% more intense currents in the NH than SH. The hemispheric differences were not statistically significant during high activity conditions. We speculated that the larger hemispheric asymmetry during low than high activity conditions might be due to differences in the local ionospheric conditions, such as background conductivity and differences in the magnetic field strength and configuration.

In this paper, we extend the analysis carried out in Paper 1 by studying the effect of seasons on the hemispheric asymmetry of FACs and horizontal currents during low and high geomagnetic activity conditions. We use five years of Swarm data, from 15 April 2014 to 14 April 2019, which is about 16 months more than in Paper 1. In data analysis, we utilize the Spherical Elementary Current Systems (SECS) data analysis method (Amm et al., 2015; Juusola et al., 2016; Vanhamäki et al., 2020) like in Paper 1. In this paper, the seasonal dependence of the hemispheric asymmetry under different geomagnetic activity is studied for the first time to our knowledge.

The rest of the paper is organized as follows. In Section 2, we briefly describe the data and data analysis methods including the bootstrap resampling method. In Section 3, we present the seasonal dependence of FACs and horizontal currents for the NH and SH. In Section 4, we present the Kp and seasonal dependence of FACs and horizontal currents for the NH and SH. In order to compare the hemispheric differences in the ionospheric background conductivity during different seasons, we calculate conductances for geomagnetically quiet conditions from the International Reference Ionosphere (IRI) model in Section 5. Finally in Section 6, we present the discussion and conclusions of the study.

2 Data analysis

2.1 Swarm data and SECS analysis method

The Swarm data set, data processing, magnetic field data analysis procedures and coordinate systems used in the analysis were explained in Paper 1, and are briefly summarised here.

In this study, we utilize data measured by Swarm A and Swarm C satellites from 15 April 2014 to 14 April 2019. Specifically, we use the level-1b calibrated 1 Hz magnetic field data (the 0505 dataset). For FAC and horizontal current estimation, we first obtain the variation magnetic field data by subtracting a background magnetic field model (CHAOS-6-x8, Finlay et al. (2016)) from measured magnetic field data. During the time we were analysing the data, the CHAOS-6-x8 was the latest extension of the CHAOS-6 model using Swarm 0505 data up to February 8, 2019 and ground observations data as available in February 2019. Note that CHAOS-6 model is a geomagnetic field model combining Earth's core, crust and magnetospheric currents.

The Spherical Elementary Current Systems (SECS) method (Amm et al., 2015; Juusola et al., 2016; Workayehu et al., 2019; Vanhamäki et al., 2020) is used to estimate FAC and horizontal currents. For estimating currents using the Swarm/SECS analysis method, we first discard magnetic data poleward of ±80° geographic latitude, where the longitudinal separation between Swarm A and C becomes too small for a reliable current estimation using this method. Then, the locations of the satellite's magnetic footpoints and the vector data are converted to Spherical-AACGM (SPH-AACGM) coordinates (see Paper 1).

The data from each orbit are divided into four overflights between [50°, 80°] and [-50°, -80°] SPH-AACGM latitudes, and we discard that part of an overflight where the satellite path is nearly parallel to the SPH-AACGM latitudes, since the analysis method fails in that situation. For each overflight, components of the magnetic field variations are fitted with the 1-dimensional (1-D) and 2-dimensional (2-D) SECS (e.g., Vanhamäki & Juusola, 2020). The 1-D SECSs describe only latitudinal variations, while the 2-D SECSs describe both latitudinal and longitudinal variations. Detailed description of the fitting procedure is given in Paper 1. Finally, the AACGM coordinate system (Shepherd, 2014) is used for binning the estimated results and calculating the statistical averages.

2.2 Division into seasons, and low and high Kp conditions

To explore the effect of seasons on the hemispheric asymmetry in FACs and ionospheric horizontal currents under different geomagnetic activity levels, we divide the oval crossings into four local seasons: NH spring and SH autumn (± 45 days around March equinox), NH summer and SH winter (± 45 days around June solstice), NH autumn and SH spring (± 45 days around September equinox), and NH winter and SH summer (± 45 days around December solstice).

In Section 4 we further group the oval crossings in each local season into two geomagnetic activity levels based on Kp index with Kp<2 and Kp≥2. All oval crossing in each season with Kp<2 are defined as the low Kp condition while the remaining data with Kp≥2 are defined as high Kp condition. With this criterion, the number of samples is roughly equal for both categories. The same criterion was used in Paper 1. Figure 1 shows the distribution of oval crossings as a function of Kp index for the four local seasons in the NH and SH. For each season, the peak of the total distribution is at Kp=1^-, and disturbed conditions with Kp $\geq$ 5 are sparse. This is consistent with the fact that the studied time interval takes place after the sunspot maximum in the declining phase of solar cycle 24.

2.3 Bootstrapping

From Figure 1, one can easily see the hemispheric differences in the Kp distribution in each local season. For example, for local winter (summer) seasons during low Kp conditions the number of oval crossings in the SH is larger (smaller) than that of the NH, while the difference is vice versa during high Kp conditions. Similarly, a small hemispheric difference is also seen in the local spring and autumn seasons (panels: b and d).

We correct for the hemispheric and seasonal differences in the Kp distributions by using bootstrap resampling (also known as bootstrapping). Bootstrapping is a statistical method that relies on random sampling with replacement from the original data (e.g., Chernick & LaBudde, 2011; Dekking & Meester, 2005). In this study, the original data are the Swarm oval crossings in each local season. In order to re-sample from the original data, we first define sampling distribution (or bootstrap distribution) according to which we randomly take samples from the original data distribution. Bootstrapping is done in such a way that the number of Swarm oval crossings in each Kp bin is the same for the four local seasons in both hemispheres. This sampling distribution is

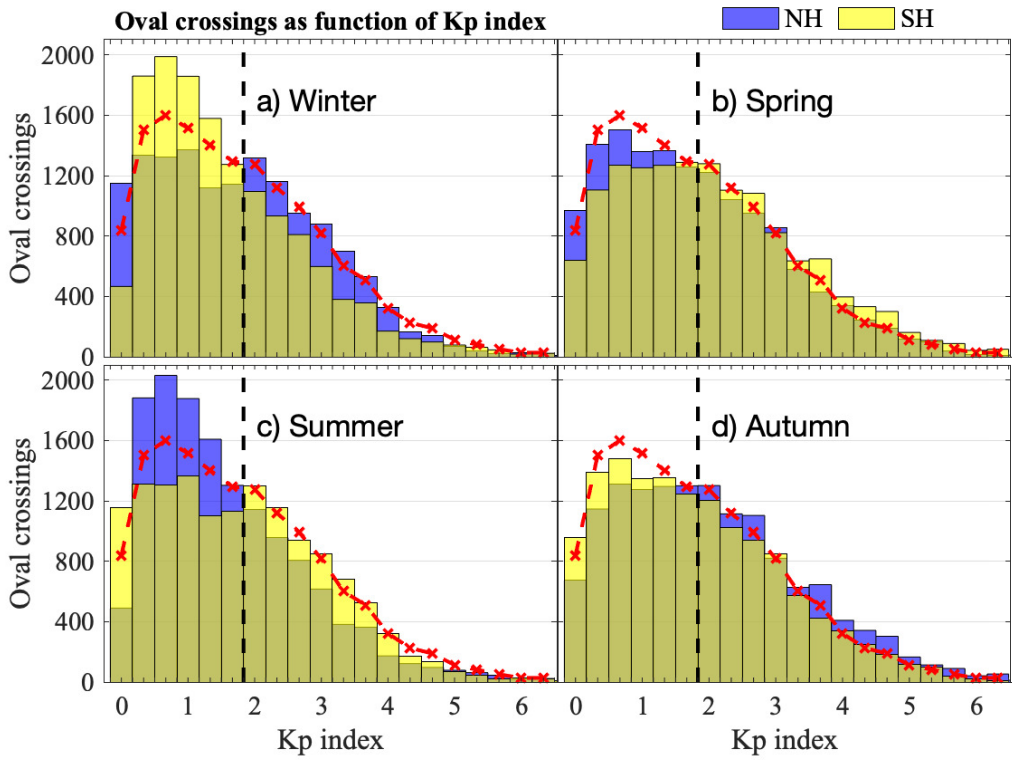

Figure 1. Distribution of Swarm oval crossings as function of Kp index for the four local seasons in the Northern (NH, blue) and Southern (SH, yellow) hemispheres. The red dashed line is the re-sampling (bootstrap) distribution of oval crossings. Oval crossings during the low Kp (Kp < 2) and high Kp (Kp≥ 2) conditions are separated by the vertical dashed line.

shown by the red dashed lines in Figure 1. For each local season, a total of 1000 bootstrap samples are randomly taken with replacement from the original data. Each bootstrap sample has the same number of oval crossings as the original dataset. Similar method was used in Paper 1 to remove the seasonal bias in the total Kp distribution, but in this study our aim is to make the seasons directly comparable to each other.

The average ionospheric horizontal currents and FACs in each 1° AACGM latitude by 1 h MLT grid cells are calculated for each of the 1000 bootstrap samples. From this, we have 1000 different distributions of the average values. Then, the median values of the average current densities in each grid cell are calculated from bootstrap statistics. These results, presented in Section 3 are our best estimates for the current densities in each grid cell.

3 Seasonal dependence

In this section we present the seasonal variation of the median FACs and horizontal currents calculated from the bootstrap statistics for all Kp values (Kp $\leq 6^{+}$). In order to quantify the seasonal and hemispheric differences in FACs and horizontal CF and DF currents, we calculate the total integrated FAC values, and the average horizontal CF and DF currents for the four local seasons using the same formula as in Paper 1, summarized below.

For each local season in each hemisphere, the total FAC value flowing between [60°, 80°] AACGM latitudes and all MLTs is obtained by

$$\mathrm{I} = \sum_{m=1}^{M} |\mathrm{FAC}_m| \mathrm{S}_m, \tag{1}$$

where FAC_m is the FAC density in grid cell m, S_m is grid cell area calculated using the AACGM coordinates and M is the total number of grid cells. The integrated FAC values contain contributions both from the upward and downward FACs.

For the CF and DF currents, we first calculate the magnitude of the current densities in each grid cell as the square root of the sum of the squares of meridional (positive southward) and zonal (positive eastward) current density components. The average CF and DF current values between [60°, 80°] are then calculated between [60°, 80°] AACGM latitudes over all MLTs using the formula

$$I = \frac{1}{M} \sum_{m=1}^{M} \Delta_{m,\phi} \sqrt{J_{m,\phi}^2 + J_{m,\theta}^2}, \tag{2}$$

where $J_{m,\theta}$ and $J_{m,\phi}$ are the meridional and zonal current density components in grid cell m, respectively, M is the total number of grid cells between [60°, 80°] AACGM latitudes and over all MLTs, while $\Delta_{m,\theta}$ is the zonal dimension of the grid cell calculated by using the AACGM coordinates.

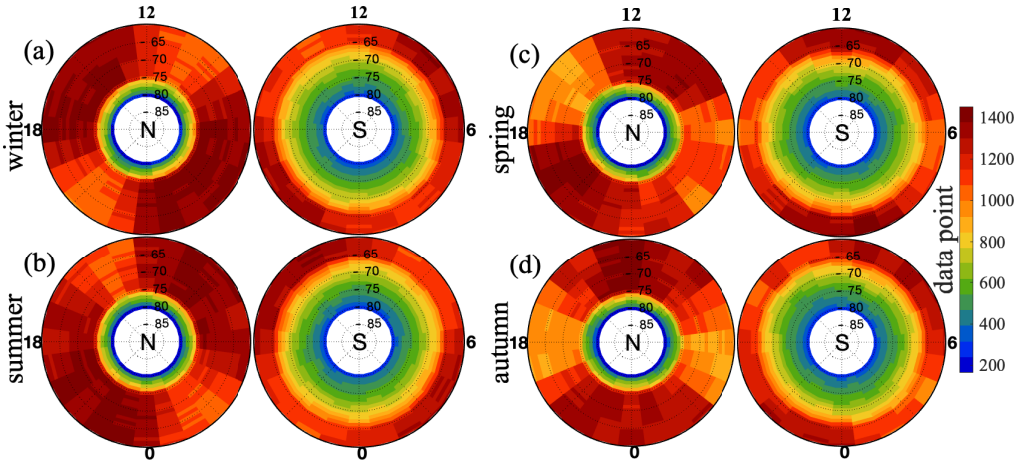

Figure 2. Bootstrapped data point distribution for the four local seasons in the NH and SH for the time period from 15 April 2014 to 14 April 2019. The plots are given in AACGM latitude by MLT.

Figure 2 shows the bootstrapped distributions of data points in the two hemispheres for the four local seasons for the whole time period. In all local seasons the NH has more data points than the SH poleward of ±66° AACGM latitude, while the SH has more samples between 60° and 65° AACGM latitudes. This is due to the difference in the locations of AACGM poles relative to the GEO poles in the two hemispheres and the Swarm A and C satellites' near polar orbits (see Figure 1 in Paper 1).

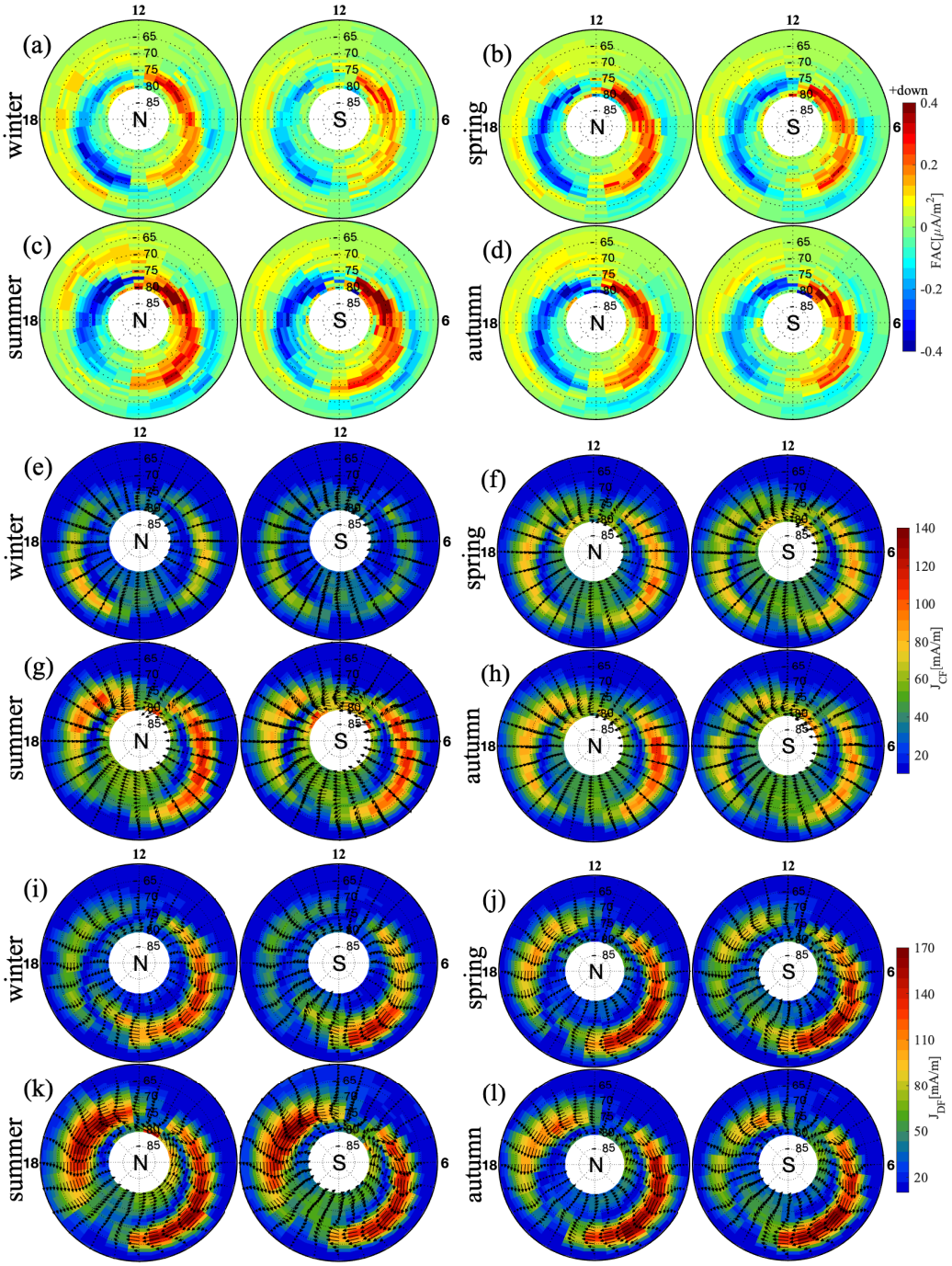

Figure 3. Distributions of median FAC density (a - d), median CF current density (e - h) and median DF current density (i - l) for the four local seasons during all ($Kp \leq 6^+$) activity conditions in the NH and SH. Downward FAC is defined positive (red color). The magnitudes and flow directions of median CF and DF currents are shown in color and arrows, respectively. The plots are given in AACGM latitude by MLT. For both hemispheres, the noon (12 MLT) is at the top and evening (18 MLT) is at the left and the lowest latitude is 60 °.

Figure 3 panels (a - d) show distributions of median FAC densities obtained with bootstrapping in both hemispheres for all four local seasons. The well known R1 and R2

current systems are clearly seen in all seasons. In both hemispheres, the dawnside FACs seem to be stronger in summer than in winter. The duskside FAC is stronger on the dayside in summer than in winter, but on the pre-midnight sector FACs in winter are stronger than in summer between 19 and 24 MLT. This is in line with previous report by Ohtani et al. (2005) who showed more intense FACs flowing in the dark (winter) than sunlit (summer) ionosphere between 20 and 02 MLTs. In order to see the seasonal variations more clearly, we compare the total integrated FACs in the local spring, autumn and summer seasons with the integrated value in the local winter for both hemispheres. The local spring, autumn and summer-to-local winter ratios and 90% confidence intervals of integrated FACs in the NH (SH) are 1.15 ± 0.04 (1.26 ± 0.06), 1.23 ± 0.04 (1.27 ± 0.06) and 1.33 ± 0.05 (1.53 ± 0.08), respectively. The summer-to-winter ratios in both hemispheres are in agreement with previous studies (e.g., Papitashvili et al., 2002; Christiansen et al., 2002; Juusola et al., 2009). Overall, the seasonal ratios in the NH and SH are not equal indicating the existence of hemispheric differences on the seasonal variations of FACs. The amplitude of the seasonal variation is larger in SH than in NH.

Figure 3 panels (e - h) show distributions of median CF currents (both magnitude and vectors) in both hemispheres for all four local seasons. The CF currents flow poleward (equatorward) in the evening (morning) sector and part of the CF current is also flowing across the polar cap from morning to evening connecting the downward R1 (morning sector) current to the upward R1 (evening sector) current. Around midnight and noon MLT sectors the CF currents flow westward and eastward, respectively. The magnitudes of the CF currents in the dusk and dawn sectors are more prominent during local summer than winter season. The only exception is winter 19-23 MLT, when CF current is stronger in winter than in summer in NH. This is in accordance with Juusola et al. (2009), who however combined data from both hemispheres. The local spring, autumn and summer to local winter ratios of average CF currents in the NH (SH) are 1.13 ± 0.03 (1.28 ± 0.03), 1.28 ± 0.03 (1.28 ± 0.03) and 1.45 ± 0.03 (1.58 ± 0.04), respectively. In the SH, the average CF current in the local autumn and spring seasons are equal, while the average CF current in the NH during autumn is larger than the current in the local spring. Visually, the hemispheric differences are more evident in the local winter and autumn seasons than local spring and summer seasons, with larger CF current intensities in the NH than SH.

Figure 3 panels (i - l) show distributions of median DF currents (both magnitude and vectors) in both hemispheres for all four local seasons. The DF currents flow eastward in the evening and westward in the morning sectors, which displays the eastward and westward electrojets, EEJ and WEJ, respectively. In the local winter seasons, an extension of the WEJ flows poleward of the EEJ current around the pre-midnight MLT sector. A reverse EEJ (sunward flowing) in the dawn MLT sector is also seen poleward of the WEJ in the local summer seasons. In both hemispheres, the seasonal variation of median DF current is clearly seen in the evening MLT sector EEJ with the smallest and largest currents in the local winter and summer season, respectively. The local spring, autumn and summer to local winter ratios of average DF currents in the NH (SH) are 1.14 ± 0.03 (1.25 ± 0.03), 1.26 ± 0.03 (1.25 ± 0.03) and 1.50 ± 0.03 (1.58 ± 0.03), respectively. Comparison of the average DF currents flowing in the dawn and dusk MLT sectors indicate that the seasonal dependence is stronger in EEJ than in WEJ. The local summer-to-winter ratio of EEJ are 1.77 ± 0.04 and 1.97 ± 0.04 in the NH and SH, respectively. These values are slightly larger than reported by Huang et al. (2017), who noticed that the value of EEJ during local summer is larger by a factor of 1.5 than the local winter. Like FACs, the ratios for DF currents in local autumn and spring indicate that stronger average current flows in the local autumn than in the local spring in the NH, while in the SH the DF current in the local spring and autumn are equal.

To show the seasonal variation in the hemispheric asymmetry in currents more clearly, we calculate the integrated FAC, average CF and DF currents, and the corresponding

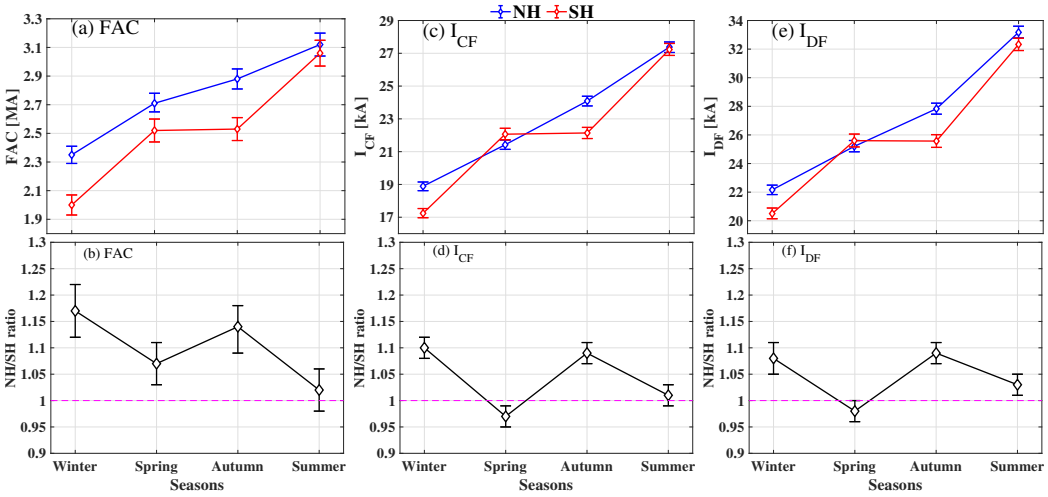

Figure 4. Median values of integrated FAC (a), average CF (c) and average DF (e) current intensities as function of seasons for all Kp conditions together in the NH and SH. The bottom panels are the median NH/SH ratios of FAC (b), CF current (d) and DF current (f). The error bars are the 90% confidence intervals.

NH/SH ratios for the four local seasons separately for each of the bootstrap samples discussed in Section 2.3. After that,we calculate the median NH/SH ratios and the corresponding 90% confidence intervals.

Figure 4 panels (a, b) show the seasonal variation of integrated FACs and median NH/SH ratios. The seasonal variation pattern of FACs is clearly different in the NH and SH. In the NH, integrated FACs in the local autumn and spring seasons are asymmetric, while they are symmetric in the SH. Comparison of values in each local season shows that larger currents are flowing in NH than in SH for winter, spring and autumn seasons, while in summer the currents in the two hemispheres are equal within the confidence level. The median NH/SH ratios in winter, spring, autumn and summer are 1.17 $\pm$ 0.05, 1.07 $\pm$ 0.04, 1.14 $\pm$ 0.05 and 1.02 $\pm$ 0.04, respectively, which indicate the hemispheric asymmetry is statistically significant in the local winter, spring and autumn seasons. The largest hemispheric asymmetry occur in winter and autumn seasons.

Figure 4 panels (c, d) show the seasonal variation of average CF currents and median NH/SH ratios. Similar to the integrated FAC values, the average CF currents show seasonal dependence with the largest and smallest currents in the local summer and winter seasons, respectively, with the values in the local spring and autumn seasons in between. In the local spring the value in SH is slightly larger than in NH, while in local autumn the current in the NH is significantly larger than SH. In the SH the local autumn and spring seasons are symmetric, but in the NH local autumn and spring seasons are asymmetric. The median NH/SH ratios of CF currents are 1.10 $\pm$ 0.02, 0.97 $\pm$ 0.02, 1.09 $\pm$ 0.02 and 1.01 $\pm$ 0.02 in winter, spring, autumn and summer, respectively. Like FACs, the largest hemispheric asymmetry occurs in winter and autumn, while the hemispheres are largely symmetric in spring and summer.

Figure 4 panels (e, f) show the seasonal variations of average DF currents and median NH/SH ratios. The seasonal variation of the average DF current has similar pattern as in the average CF current, with the largest and smallest currents in the local summer and winter seasons, respectively. In the SH the local autumn and spring seasons the DF currents are symmetric, but in the NH the average DF currents in the local autumn and spring seasons are asymmetric. The median NH/SH ratios are 1.08 $\pm$ 0.03, 0.98 $\pm$

0.02, 1.09 and 1.03 ± 0.02 in winter, spring, autumn and summer seasons, respectively. Like for FACs and horizontal CF currents, the largest hemispheric asymmetry in the horizontal DF currents occurs in winter and autumn.

4 Kp and seasonal dependence

In Paper 1 we showed that the hemispheres are asymmetric for low (Kp<2) activity conditions, while the hemispheres are largely symmetric during geomagnetically active conditions (Kp $\geq$ 2). Now we study how the geomagnetic activity effects are seen during different seasons. Section 3 showed that the largest NH/SH asymmetry occurs in winter and autumn, and the smallest in summer and spring within the studied five years period. The current values are most intense in summer and weakest in winter. Therefore, we have selected winter and summer seasons for plots showing the full magnetic latitude - MLT distributions of currents during low (Kp $<$ 2) and high (Kp $\geq$ 2) geomagnetic activity conditions in Figure 5.

Figure 5 panels (a-d) show the distributions of median FACs in the local winter and summer seasons during low (a, b) and high (c, d) geomagnetic activity conditions in the NH and SH. As expected, FAC densities become stronger and the oval expands equatorward as the activity changes from low to high, during both local winter and summer seasons. Visually, the FAC densities seem to be significantly stronger in the NH than in the SH during local winter under low activity conditions, while in the local summer, the FAC densities in the two hemispheres seem to be quite similar under both low and high activity conditions.

Figure 6 quantifies the magnitudes of currents and NH/SH ratios. Figure 6 panels (a, b) show the seasonal variations of integrated FACs in the NH and SH during low (a) and high (b) activity conditions for all the four seasons. Here, the seasonal variation of FAC is clearly seen with the largest and smallest currents in the local summer and winter, respectively. The error bars are the 90% confidence ranges. During low activity conditions, the error bars for the local winter, spring and autumn are not overlapping. This indicates statistically significant hemispheric difference in these seasons, with larger FAC flowing in the NH than SH. The hemispheric difference is larger during low Kp conditions. The seasonal patterns of FAC variations in the NH and SH are more similar during low than high activity conditions. In the NH the local autumn and local spring are more asymmetric during high than low activity conditions. In the SH the integrated FAC during local autumn and spring seasons are equal.

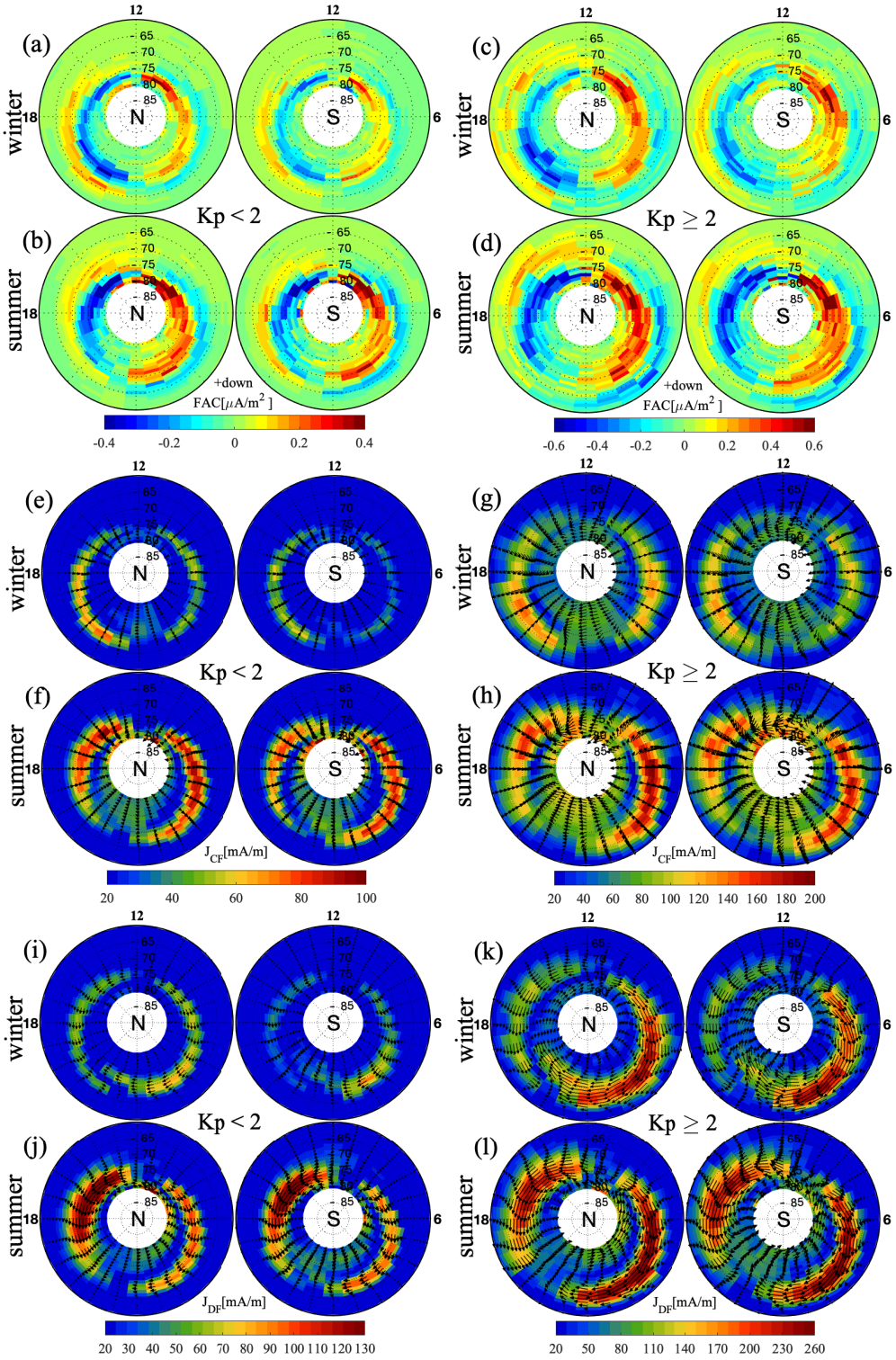

Figure 5. Distributions of median FAC density (a-d), median CF current density (e-h) and median DF current density (i-l) for the local winter and summer seasons during low (Kp<2, left panels) and high (Kp≥ 2, right panels) activity conditions in the NH and SH. The magnitudes and flow directions of median CF and DF currents are shown in color and arrows, respectively. Note that the color scales for low and high activity levels are different.

Figure 6 panel (c) shows the seasonal variation of the median NH/SH ratios and the corresponding 90% confidence range of FACs obtained from bootstrapping for both low (solid line) and high (dashed line) magnetic activity conditions. Panel 6 (c) confirms the visual inspection of Figure 5 that during winter the NH/SH ratio is higher for low than for high Kp conditions. The values of the median NH/SH ratios during low (high) activity conditions are 1.21 ± 0.06 (1.06 ± 0.05) in winter, 1.12 ± 0.05 (1.02 ± 0.05) in spring, 1.17 ± 0.06 (1.08 ± 0.06) in autumn and 1.01 ± 0.05 (1.00 ± 0.04) in summer. The hemispheric asymmetry is statistically significant in winter, spring and autumn for low Kp conditions, and in winter and autumn for high Kp conditions. As shown in Table 1, much of the hemispheric asymmetry during low Kp conditions from the evening MLT sector. For example, in winter the FAC in the NH is stronger than in the SH by a factor of 1.13 in the MLT range between 1 and 12, while in the MLT range between 13 and 24 the NH is 1.28 times stronger than the SH. In summary, the values of the NH/SH ratios confirm that the hemispheric asymmetry is larger during low than high activity conditions, which is in accordance of the results reported in Paper 1 for all seasons together.

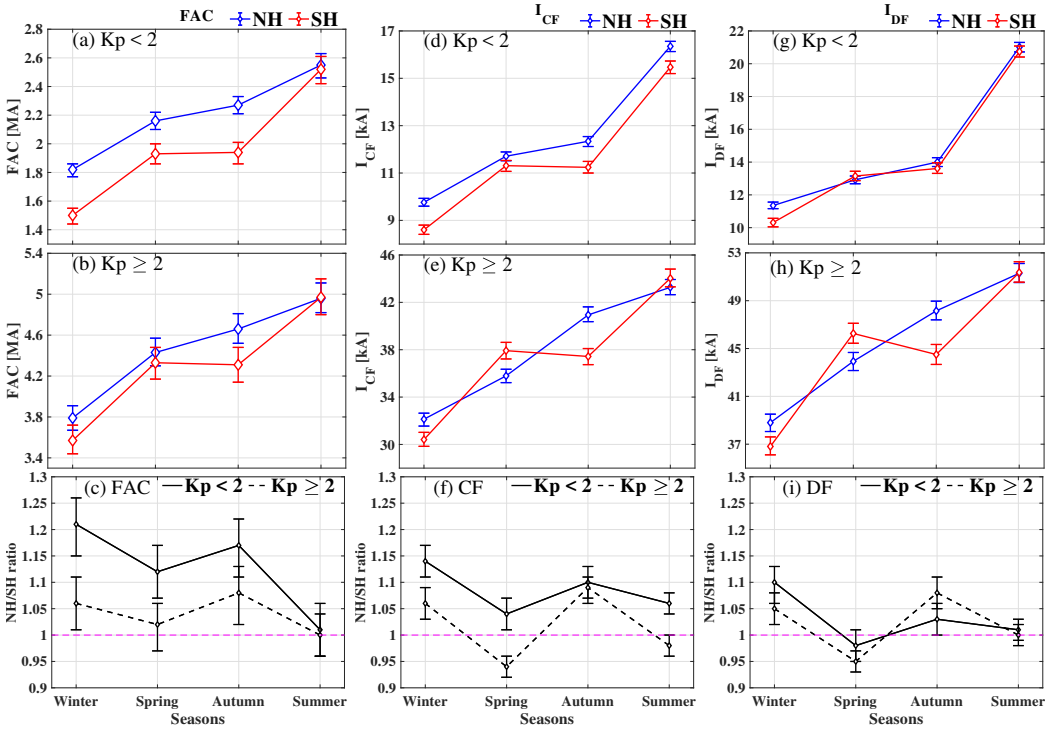

Figure 6. Median values of integrated FAC (a, b), average CF (d, e) and average DF (g, h) currents as function of season during low (Kp <2, upper panels) and high (Kp ≥ 2, middle panels) activity levels. The bottom panels show the median NH/SH ratios of FAC (c), CF current (f) and DF current (i) for the four local seasons during low Kp (solid lines) and high Kp (dashed lines) conditions.

Figure 5 panels (e-h) show the distributions of median CF currents during low (e, f) and high (g, h) activity conditions in the NH and SH during winter and summer. In both hemispheres, the median CF current densities both in the dusk and dawn MLT sectors intensify and expand to lower latitudes as the geomagnetic activity changes from low to high conditions. Like for FACs, large hemispheric difference occurs in winter dur-

ing low activity conditions with larger median CF current density in the NH than in the SH.

Figure 6 panels (d, e) show the seasonal variations of the average CF currents in the NH and SH during low (d) and high (e) geomagnetic activity conditions for all seasons. During low activity conditions larger average CF currents are flowing in the NH than in the SH for all local seasons. During high activity conditions the average CF currents are larger in the NH for local winter and autumn, while the currents are larger in the SH in the local spring and summer seasons.

Figure 6 panel (f) shows the median NH/SH ratios of the horizontal CF currents as a function of local seasons during low and high activity conditions. During low activity conditions, the values of the median ratios are 1.14 ± 0.03 in winter, 1.04 ± 0.05 in spring, 1.10 ± 0.05 in autumn and 1.06 ± 0.05 in summer. Table 1 shows that much of the hemispheric differences come from the evening MLT sector. Like for FACs, the largest asymmetry occurs in winter and autumn seasons. During high activity conditions, the NH/SH ratios are 1.06 ± 0.03, 0.94 ± 0.02, 1.09 ± 0.03 and 0.98 ± 0.02 in winter, spring, autumn and summer, respectively. In this case, the largest hemispheric asymmetry is observed in autumn, and the average CF current in spring is larger in the SH than in the NH.

Figure 5 panels (i-l) show the distributions of the median DF currents during low (i, j) and high (k, l) activity conditions in the NH and SH during winter and summer. In both hemispheres, the WEJ intensifies more than the EEJ as the activity changes from low to high conditions. Like FACs and CF currents, clear hemispheric difference in the median DF currents occur in winter under low activity conditions, with larger current density in the NH than SH. Apart from the hemispheric differences in the magnitudes of DF currents, an interesting winter-summer difference is observed in both hemispheres between 19 and 23 MLTs, which is the Harang discontinuity region. In the local winter, an overlap between EEJ and WEJ with sharp latitudinal separation occurs during both low and high activity conditions and in both hemispheres, with the WEJ extending to the premidnight sector poleward of the EEJ. In contrast, during summer the EEJ and WEJ are separated longitudinally, and there is no clear overlap between EEJ and WEJ around the Harang discontinuity region. These two configurations may correspond to the expansion-type and rotation-type Harang discontinuities discussed by Amm et al. (2000).

NH/SH ratios of currents during Kp < 2 for different MLT sectors									
Seasons	FAC			I_{CF}			I_{DF}		
	1-24 MLT	1-12 MLT	13-24 MLT	1-24 MLT	1-12 MLT	13-24 MLT	1-24 MLT	1-12 MLT	13-24 MLT
Winter	1.21	1.13	1.28	1.14	1.15	1.12	1.10	1.06	1.14
Spring	1.12	1.09	1.15	1.04	1.02	1.05	0.98	0.96	1.01
Summer	1.01	1.01	1.01	1.06	1.03	1.08	1.01	0.92	1.09
Autumn	1.17	1.09	1.26	1.10	1.04	1.15	1.03	0.92	1.15

Table 1. Median NH/SH ratios of FACs, horizontal CF and DF currents for different MLT sectors during low Kp conditions.

Figure 6 panels (g, h) show the seasonal variations of the average DF currents in the NH and SH during low (g) and high (h) activity conditions for all seasons. During

low activity conditions, larger average DF currents are flowing in the NH than SH for local winter, while in the other local seasons the average DF currents are largely symmetric between the hemispheres. During high activity conditions the average DF current is larger in the SH for local spring, while larger DF currents are flowing in the NH than in the SH for local winter and autumn. In the local summer the average DF currents from the two hemispheres are equal.

Figure 6 panel (i) shows the median NH/SH ratios of the horizontal DF currents as a function of local seasons during low and high activity conditions. In the low activity conditions, the NH/SH ratios are 1.10 $\pm$ 0.04 in winter, 0.98 $\pm$ 0.03 in spring, 1.03 $\pm$ 0.03 in autumn and 1.01 $\pm$ 0.02 in summer. These values indicate that the largest hemispheric asymmetry occurs in winter, while the hemispheres are symmetric in the other seasons within uncertainty limits. As shown in Table 1, most of the hemispheric asymmetry in the median DF current in winter comes from the EEJ, with only little hemispheric difference in the WEJ. In the evening sector, the EEJ in the NH is larger than in the SH by a factor of 1.14. Also in autumn, a significant hemispheric asymmetry exists in the evening sector with the EEJ in the NH is larger than in the SH by a factor of 1.15. During the high activity case, the NH/SH ratios of DF currents are 1.05 $\pm$ 0.03 in winter, 0.95 $\pm$ 0.02 in spring, 1.08 $\pm$ 0.03 in autumn and 1.00 $\pm$ 0.02 in summer. The NH/SH values indicate that the largest hemispheric asymmetry occurs in autumn with larger DF current in the NH than in the SH. Like for CF currents, the median NH/SH is < 1 indicating that the DF currents are larger in the SH than in the NH in spring.

5 Conductances from IRI and NRLMSISE models

Ionospheric conductivity affects the electromagnetic coupling between the ionosphere and magnetosphere (Newell et al., 1996). In Paper 1, we speculated that background conductivity during low Kp conditions may play a role in inter-hemispheric asymmetry of currents. The high latitude ionospheric conductivities are produced by the solar extreme ultraviolet (EUV) radiation and precipitating energetic particles. Ionization due to solar EUV radiation depends smoothly on the solar zenith angle, while particle precipitation varies rapidly both in space and time depending on the geomagnetic activity level (e.g., Sheng et al., 2014). The electric conductivity due to these ionization processes depends also on the atmospheric composition and magnetic field strength.

Under quiet geomagnetic conditions ionospheric conductivity due to precipitating particles is relatively small, so in the dayside the ionospheric conductivity variations are dominated by solar illumination. During nighttime, the solar induced ionization in the E-region decays rapidly, and the conductance variations are dominated by precipitation.

We calculate the height integrated Pedersen (Σ_P) and Hall (Σ_H) conductivities for one representative day per local season under similar geomagnetic and solar activity conditions. We use the results to asses the degree of asymmetry in the ionospheric conductivities between the NH and SH. The electron and ion density profiles are taken from the International Reference Ionosphere (IRI-2016) model (Bilitza et al., 2017), and the neutral density profiles are calculated from the Naval Research Laboratory Mass Spectrometer Incoherent Scatter Radar (NRLMSISE-00) model (Picone et al., 2002). The input parameters to the IRI-2016 and NRLMSISE-00 models are location, date and time, as well as the F10.7, F10.7a, Ap indices and the sunspot number (Rz). We run the two models for geomagnetically quiet conditions using the following values: F10.7=40 sfu, F10.7a=40 sfu, Ap=3 (which is equal to Kp=1^-), and Rz=30. The resulting Hall and Pedersen conductivities are height-integrated in the altitude range 90-200 km. Detailed description of the conductivity calculation and height-integration are given in the Appendix.

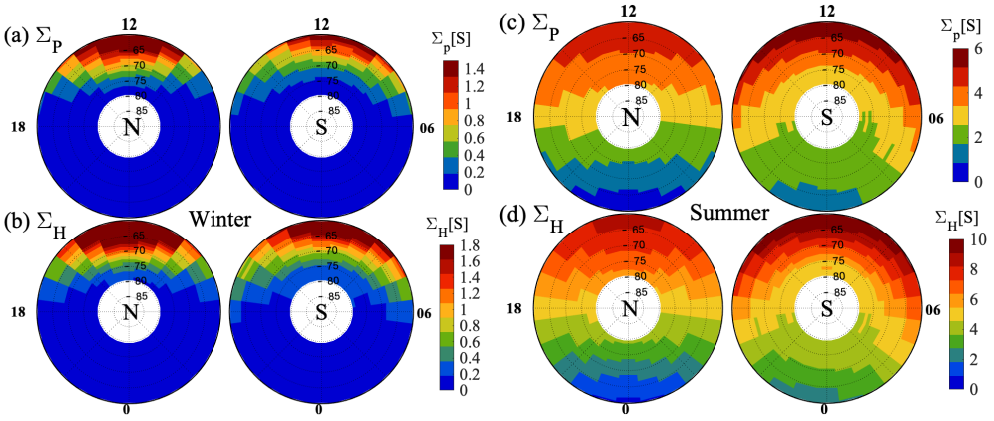

Figure 7. Height integrated Pedersen (top panels) and Hall (bottom panels) conductivities in Siemens (S) during local winter (a, b) and summer (c, d) solstices in the NH and SH in AACGM latitude and MLT coordinates averaged over 00-24 UT. Note that the color scales in (a) and (b) as well as (c) and (d) are different.

Figure 7 illustrates distributions of the Pedersen and Hall conductances averaged over 00-24 UT for the local winter and summer solstices in the NH and SH. In both local winter and summer solstices, conductivities are highest on the dayside at the lowest latitudes. However, the latitudinal and MLT distributions of conductances are different in different hemispheres. In the local winter, the maximum conductances are higher in the NH than in the SH, while in the local summer, the maximum values are higher in the SH than in the NH. In the local winter solstices, the conductances are very small and in the night sector (18–06 MLT) both Pedersen and Hall conductances are below 0.2 S. Furthermore, the auroral oval is not visible in conductances, neither during winter nor summer solstice.

The hemispheric difference in the solar EUV produced conductances, which seem to dominate the IRI results, can be attributed to several factors. One of the factor is that the Earth receives more sunlight in December solstice (NH winter/SH summer) than in June solstice (NH summer/SH winter) due to the change in the Sun-Earth distance. The Earth receives about 7% more solar radiation flux in December solstice than in June solstice, which leads to about 3 % difference in the E-region electron density (assuming α-type recombination), and would result in the NH/SH ratio of 1.03 for winter and 0.97 for summer. Moreover, higher conductance in the SH than in the NH may also be due to the larger offset between geographic and magnetic poles. The SH magnetic pole lies at a lower geographic latitude than NH magnetic pole, resulting in larger diurnal variations of the solar zenith angle and greater ionospheric conductances on average in the SH high-latitude (60°- 80°). The weaker magnetic field strength in the SH high-latitude region (60°- 80°) also results in larger conductance in the SH than in the NH for similar solar zenith angles (see Equations A.1 and A.2).

The seasonal variations as well as the hemispheric asymmetry of conductances are more clearly seen from the average values and the corresponding NH/SH ratios. Table 2 shows the weighted average Pedersen and Hall conductances for all local seasons. They are calculated as

$$\langle \Sigma \rangle = \frac{1}{S} \sum_{m=1}^{M} \Sigma_{\mathrm{m}} \mathrm{S}_m, \tag{3}$$

where Σ_m is conductance in grid cell m, S_m is area of grid cell and $\mathrm{S}=\sum_{m=1}^{M} \mathrm{S}_m$. In both hemispheres, the average conductances vary with season with the smallest and largest

values in the local winter and summer solstices, respectively. This is due to the fact that the solar irradiance, which seems to be the dominant cause for high latitude ionospheric electron density during low geomagnetic activity condition in the IRI model, has a strong dependence on seasons. The conductances are larger in the NH than in the SH during local winter and autumn seasons, while in the local spring and summer the values are larger in the SH than in the NH. The average values of Pedersen and Hall conductances in winter given by the model seem to be too small (< 0.5 S) to support realistic ionospheric currents. This may be related to the fact that the auroral oval caused by particle precipitation is not reproduced in the model. In each hemisphere, the average conductances in the local spring and autumn are not identical. In the NH, the conductances in the local autumn are larger than in spring, while in the SH, the conductances are slightly larger in the local spring than in autumn. The larger spring-autumn asymmetry in the NH than in the SH seems in accordance with the spring-autumn asymmetries seen on the FACs and horizontal currents, which we have discussed in Sections 3 and 4.

In order to quantify the extent of the seasonal variations of conductances in each hemisphere, we take the difference of the average values between the local summer and winter solstices. The summer-winter difference of Pedersen (Hall) conductances in the NH are 2.65 S (4.67 S), while the values are 2.99 S (5.23 S) in the SH. The seasonal variations in both Pedersen and Hall conductances are larger in the SH than in the NH. This is also in line with the result reported in Section 3 that the seasonal variation in auroral currents is larger in the SH than in the NH.

Average conductances within 60°- 80° AACGM latitude for Kp= 1^-, F10.7=40								
	Winter		Spring		Autumn		Summer	
	$\langle\Sigma_P\rangle$	$\langle\Sigma_H\rangle$	$\langle\Sigma_P\rangle$	$\langle\Sigma_H\rangle$	$\langle\Sigma_P\rangle$	$\langle\Sigma_H\rangle$	$\langle\Sigma_P\rangle$	$\langle\Sigma_H\rangle$
NH	0.26	0.44	1.25	2.16	1.47	2.65	2.91	5.11
SH	0.23	0.43	1.38	2.26	1.25	2.19	3.22	5.66
NH/SH	1.13	1.02	0.91	0.96	1.18	1.21	0.90	0.90

Table 2. Average Pedersen and Hall conductances in Siemens (S), and the corresponding NH/SH ratios for the four local seasons during low activity condition.

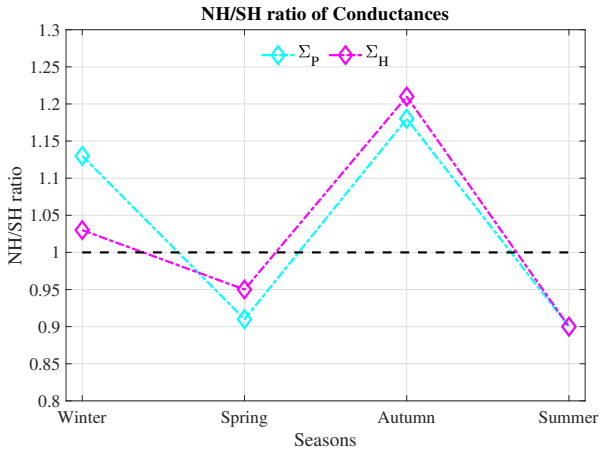

Figure 8. The NH/SH ratios of average conductances for the four local seasons.

Figure 8 shows the NH to SH ratios of average Pedersen and Hall conductances. The NH/SH ratios of both the Pedersen and Hall conductance have the largest values in autumn and winter seasons and smallest values in summer and spring. This is in agreement with the hemispheric asymmetry in the FACs and horizontal CF and DF currents during low activity conditions (see Figure 6). However, the peak NH/SH ratio of about 1.2 for both conductances is in autumn, while for low Kp conditions, the peak value both for FACs and horizontal currents comes always in winter (Figure 6).

Overall, the NH/SH ratios seem to indicate the presence of hemispheric difference in average conductances. However, the average values of conductances estimated from the IRI model, especially in winter, are too small to support realistic ionospheric currents. In addition, the nighttime conductances are very small and the auroral oval is not reproduced by the model during any local season. Certainly, the smaller nighttime conductance values and the missing auroral oval limit the reliability of the results. However, these calculations still indicate that there are some hemispheric differences in the average conductances, but they do not seem to fully explain the observed hemispheric asymmetries in the currents.

6 Discussion and conclusions

In this paper, we have investigated the effect of seasons on the hemispheric asymmetry of FACs and ionospheric horizontal currents during low and high magnetic activity conditions using five years of Swarm vector magnetic field measurements. We find that both the seasons and geomagnetic activity level affect the hemispheric asymmetry in currents.

The most important findings of this paper are the following:

- Considering all data with Kp $< 6^+$, hemispheric asymmetry in auroral currents is largest in winter and autumn and smallest in summer and spring. The NH/SH ratio for FACs in winter, autumn, spring and summer are 1.17 ± 0.05, 1.14 ± 0.05, 1.07 ± 0.04 and 1.02 ± 0.04, respectively.
- NH/SH ratios during all seasons for FACs and in most cases for horizontal currents are higher for low Kp (< 2) than high Kp (≥ 2) conditions. This is in accordance with Paper 1.
- In Paper 1, we found that for high Kp conditions and all seasons together, the NH/SH ratio for currents was about 1, when the uncertainty limits were taken into account. However, now we find that also for high Kp, the NH/SH ratio is above 1 in winter and autumn with statistical significance.
- Evening sector contributes more to the high NH/SH ratio than the morning sector. For example, for low Kp conditions and for FACs, the NH/SH ratio for 13-24 MLT is 1.28 (1.26) in winter (autumn) and for 01-12 MLT 1.13 (1.09) in winter (autumn).
- Summer-to-winter ratio of FACs is 1.33 in NH and 1.53 in SH. For horizontal CF and DF currents, summer-to-winter ratio values range from 1.45 to 1.58. All values are in accordance with earlier studies of summer-to-winter ratios. However, it is worth noticing that the amplitude of the seasonal variations in auroral currents is larger in the SH than in the NH.
- In the NH the currents are stronger in autumn than spring, with autumn-to-spring ratios 1.06 for FAC, 1.12 for CF and 1.10 for DF currents. In the SH, auroral currents in spring and autumn are equal.
- Seasonal dependence is stronger in the EEJ than in the WEJ: the summer-to-winter ratios of EEJ (WEJ) are 1.77 (1.26) and 1.97 (1.26) in the NH and SH, respectively. This may be related to the fact that the EEJ is dominated by convection

electric field, and hence the role of the background conductivity can be expected to play a larger role than for WEJ, which is dominated by conductivity produced by electron precipitation (Kamide & Kokubun, 1996).

The physical mechanisms producing the hemispheric asymmetry are not presently understood. However, the fact that the observed hemispheric asymmetry depends both on local seasons and geomagnetic activity conditions suggest that both the local ionospheric conditions, such as magnetic field strength or daily variations in insolation, as well as external forcing from the magnetosphere associated with orientations of the IMF components may play a role.

We calculated the background ionospheric conductances during low magnetic activity conditions from the IRI, NRLMSISE and CHAOS models in Section 5 in order to understand the role of local ionospheric conditions on the hemispheric asymmetry. The results show seasonal variations of conductances in both hemispheres, which interestingly produces NH/SH ratios having maxima in local winter and autumn. However, the average conductance values are too small to support flow of significant ionospheric current in the local winter season during the nighttime. Moreover, background ionospheric conductances based on the IRI model don't reproduce conductivities due to precipitation in the auroral oval. The results indicate that only a small part of the seasonal dependence in the NH/SH total current ratios can be explained by variations in the background solar induced conductances.

Recent statistical studies (e.g., Laundal & Østgaard, 2009; Østgaard & Laundal, 2013; Østgaard et al., 2015, and references therein) have shown hemispheric asymmetries in the auroral intensities. These are obviously related to particle precipitation and associated conductance enhancements. The asymmetric auroral intensities are also attributed to hemispheric differences in the solar wind dynamo efficiency when the IMF has a significant B_x component. In their review paper, Østgaard et al. (2015) reported that the auroral intensity is stronger in the NH (SH) with $B_x < 0$ ($B_x > 0$).

In addition to ionospheric conductances, the FACs and horizontal currents are related to the electric field imposed on the ionosphere by the ionosphere-magnetosphere coupling as well as IMF B_y polarity. Pettigrew et al. (2010) have conducted a statistical study on the dipole tilt angle dependency, which is related to seasonal variations, and hemispheric symmetry of the high-latitude convection pattern and cross polar cap potential using Super Dual Auroral Radar Netwok (SuperDARN) measurements. Their result show that when the hemispheres are compared under opposite signs of IMF B_y, the cross polar cap potential of the hemisphere with IMF B_y <0 is larger. Using data from POGO, Magsat, CHAMP, and Swarm, Smith et al. (2017) have found a seasonal dependent hemispherical asymmetry response of auroral electrojet to the polarity of IMF B_y. They found stronger (weaker) auroral electrojet currents in the NH than in the SH during $B_y > 0$ ($B_y < 0$) around the local winter. However, they didn't find significant B_y effect on the auroral electrojet in the local summer season.

Hence, external forcing related to hemispherically asymmetric particle precipitations and magnetospheric convection electric field is likely to contribute to the hemispheric asymmetry in the FACs and ionospheric horizontal currents. In the next paper we will investigate the effect of IMF on the hemispheric asymmetry of auroral current systems in order to further gauge the conditions where significant asymmetries appear.

Appendix: Formulae for conductance calculation

The altitude profiles of Pedersen and Hall conductivities are calculated using the following formulae

$$\sigma_P = \frac{eN_e}{B}\left[\frac{\nu_{en}\Omega_e}{\nu_{en}^2+\Omega_e^2} + r_{i1}\frac{\nu_{in1}\Omega_{i1}}{\nu_{in1}^2+\Omega_{i1}^2} + r_{i2}\frac{\nu_{in2}\Omega_{i2}}{\nu_{in2}^2+\Omega_{i2}^2} + r_{i3}\frac{\nu_{in3}\Omega_{i3}}{\nu_{in3}^2+\Omega_{i3}^2}\right] \tag{A.1}$$

and

$$\sigma_H = \frac{eN_e}{B}\left[\frac{\Omega_e^2}{\nu_{en}^2+\Omega_e^2} - r_{i1}\frac{\Omega_{i1}^2}{\nu_{in1}^2+\Omega_{i1}^2} - r_{i2}\frac{\Omega_{i2}^2}{\nu_{in2}^2+\Omega_{i2}^2} - r_{i3}\frac{\Omega_{i3}^2}{\nu_{in3}^2+\Omega_{i3}^2}\right], \tag{A.2}$$

where e is the electron charge, B is the magnetic field, N_e is the electron density, Ω_e is the electron gyro frequency, Ω_i is the ion gyro frequency, ν_{en} is the electron-neutral collision frequency and ν_{inj} are the ion-neutral collision frequencies for three ion species $j = 1, 2, 3$, which are NO^+, O_2^+ and O^+, respectively. The relative contributions of these ions are $r_{ij}\ \varepsilon\ [0, 1]$. The CHAOS-6 model is used to calculate the magnetic field.

The electron-neutral and ion-neutral collision frequencies are calculated using the formula given by Schunk and Nagy (2009) as follows, where the three most important neutral species O_2, N_2 and O are included.

$$\begin{aligned}\nu_{en} &= 2.33\times10^{-17}\times n(N_2)\times\left[1-1.21\times10^{-4}\times T_e\right]\times T_e \\ &+ 1.82\times10^{-16}\times n(O_2)\times\left[1+3.6\times10^{-2}\times\sqrt{T_e})\right]\times\sqrt{T_e} \\ &+ 8.9\times10^{-17}\times n(O)\times\left[1+5.7\times10^{-4}\times T_e\right]\times\sqrt{T_e}\end{aligned} \tag{A.3}$$

$$\begin{aligned}\nu_{in1} &= 4.34\times10^{-16}\times n(N_2) + 4.27\times10^{-16}\times n(O_2) \\ &+ 2.44\times10^{-16}\times n(O)\end{aligned} \tag{A.4}$$

$$\begin{aligned}\nu_{in2} &= 4.13\times10^{-16}\times n(N_2) + 2.31\times10^{-16}\times n(O) \\ &+ 2.59\times10^{-17}\times n(O_2)\times\sqrt{T_r}\times\left(1-0.073\times\log_{10}(T_r)\right)^2\end{aligned} \tag{A.5}$$

$$\begin{aligned}\nu_{in3} &= 6.82\times10^{-16}\times n(N_2) + 6.66\times10^{-16}\times n(O_2) \\ &+ 3.67\times10^{-17}\times n(O)\times\sqrt{T_r}\times\left(1-0.064\times\log_{10}(T_r)\right)^2,\end{aligned} \tag{A.6}$$

where n(N_2), n(O_2) and n(O) are number densities of N_2, O_2 and O, respectively, T_e, T_i and T_n are electron, ion and neutral temperatures, respectively, and $T_r = \frac{T_i+T_n}{2}$.

The Pedersen and Hall conductances are height integrated as

$$\Sigma_P = \sum_{k=1}^{N}\sigma_P(z_k)\delta z \tag{A.7}$$

and

$$\Sigma_H = \sum_{k=1}^{N}\sigma_H(z_k)\delta z \tag{A.8}$$

where N is the number of altitudes between 90 and 200 km and δz is the altitude resolution. In our calculation δz was 2 km.

Acknowledgments

This work was supported by the Academy of Finland (projects 314664 and 285474). The European Space Agency (ESA) is acknowledged for providing the Swarm data. The calibrated 1 Hz Swarm magnetic field data are available at `ftp://swarm-diss.eo.esa.int`. The Kp index data used in this study are available at `http://isgi.unistra.fr`. These data are calculated and made available by the GFZ German Research Centre for Geosciences from data collected at magnetic observatories. We thank the involved national institutes, the INTERMAGNET network and the International Service of Geomagnetic Indices. The CHAOS-6-x8 model is available at `http://www.spacecenter.dk/files/magnetic-models/CHAOS-6`. The Altitude adjusted corrected geomagnetic (AACGM) coordinate transformation software is available at `http://superdarn.thayer.dartmouth.edu/aacgm.html`. The authors greatly appreciate the availability of the software from these websites.

References

Amm, O., Janhunen, P., Opgenoorth, H. J., Pulkkinen, T. I., & Viljanen, A. (2000). Ionospheric shear flow situations observed by the miracle network, and the concept of harang discontinuity. In *Magnetospheric current systems* (p. 227-236). American Geophysical Union (AGU). Retrieved from `https://agupubs.onlinelibrary.wiley.com/doi/abs/10.1029/GM118p0227` doi: 10.1029/GM118p0227

Amm, O., Vanhamäki, H., Kauristie, K., Stolle, C., Christiansen, F., Haagmans, R., ... Escoubet, C. P. (2015). A method to derive maps of ionospheric conductances, currents, and convection from the Swarm multisatellite mission. *Journal of Geophysical Research: Space Physics*, *120*(4), 3263–3282. Retrieved from `http://dx.doi.org/10.1002/2014JA020154` (2014JA020154) doi: 10.1002/2014JA020154

Bilitza, D., Altadill, D., Truhlik, V., Shubin, V., Galkin, I., Reinisch, B., & Huang, X. (2017). International reference ionosphere 2016: From ionospheric climate to real-time weather predictions. *Space Weather*, *15*(2), 418–429. Retrieved from `http://dx.doi.org/10.1002/2016SW001593` (2016SW001593) doi: 10.1002/2016SW001593

Chernick, M. R., & LaBudde, R. A. (2011). *An introduction to Bootstrap methods with applications to R.* Thomas Jefferson University, US: John Wiley Sons, Inc.

Christiansen, F., Papitashvili, V. O., & Neubert, T. (2002). Seasonal variations of high-latitude field-aligned currents inferred from ørsted and Magsat observations. *Journal of Geophysical Research: Space Physics*, *107*(A2), SMP 5-1–SMP 5-13. Retrieved from `http://dx.doi.org/10.1029/2001JA900104` doi: 10.1029/2001JA900104

Coxon, J. C., Milan, S. E., Carter, J. A., Clausen, L. B. N., Anderson, B. J., & Korth, H. (2016). Seasonal and diurnal variations in AMPERE observations of the birkeland currents compared to modeled results. *Journal of Geophysical Research: Space Physics*, *121*(5), 4027–4040. Retrieved from `http://dx.doi.org/10.1002/2015JA022050` (2015JA022050) doi: 10.1002/2015JA022050

Dekking, C. L. H., F.M. Kraaikamp, & Meester, L. (2005). *A modern introduction to probability and statistics.* Springer-Verlag London: Springer-Verlag London.

Finlay, C. C., Olsen, N., Kotsiaros, S., Gillet, N., & Tøffner-Clausen, L. (2016, Jul 11). Recent geomagnetic secular variation from Swarm and ground observatories as estimated in the CHAOS-6 geomagnetic field model. *Earth, Planets and Space*, *68*(1), 112. Retrieved from `https://doi.org/10.1186/s40623-016-0486-1` doi: 10.1186/s40623-016-0486-1

Fujii, R., Iijima, T., Potemra, T. A., & Sugiura, M. (1981). Seasonal dependence

of large-scale birkeland currents. *Geophysical Research Letters*, *8*(10), 1103-1106. Retrieved from https://agupubs.onlinelibrary.wiley.com/doi/abs/10.1029/GL008i010p01103 doi: 10.1029/GL008i010p01103

Green, D. L., Waters, C. L., Anderson, B. J., & Korth, H. (2009). Seasonal and interplanetary magnetic field dependence of the field-aligned currents for both Northern and Southern Hemispheres. *Annales Geophysicae*, *27*(4), 1701–1715. Retrieved from https://www.ann-geophys.net/27/1701/2009/ doi: 10.5194/angeo-27-1701-2009

Huang, T., Lühr, H., & Wang, H. (2017). Global characteristics of auroral Hall currents derived from the Swarm constellation: dependences on season and IMF orientation. *Annales Geophysicae*, *35*(6), 1249–1268. Retrieved from https://www.ann-geophys.net/35/1249/2017/ doi: 10.5194/angeo-35-1249-2017

Juusola, L., Kauristie, K., Amm, O., & Ritter, P. (2009). Statistical dependence of auroral ionospheric currents on solar wind and geomagnetic parameters from 5 years of CHAMP satellite data. *Annales Geophysicae*, *27*(3), 1005–1017. Retrieved from https://www.ann-geophys.net/27/1005/2009/ doi: 10.5194/angeo-27-1005-2009

Juusola, L., Kauristie, K., Vanhamäki, H., Aikio, A., & van de Kamp, M. (2016). Comparison of auroral ionospheric and field-aligned currents derived from Swarm and ground magnetic field measurements. *Journal of Geophysical Research: Space Physics*, *121*(9), 9256–9283. Retrieved from http://dx.doi.org/10.1002/2016JA022961 (2016JA022961) doi: 10.1002/2016JA022961

Kamide, Y., & Kokubun, S. (1996). Two-component auroral electrojet: Importance for substorm studies. *Journal of Geophysical Research: Space Physics*, *101*(A6), 13027-13046. Retrieved from https://agupubs.onlinelibrary.wiley.com/doi/abs/10.1029/96JA00142 doi: 10.1029/96JA00142

Laundal, K. M., Cnossen, I., Milan, S. E., Haaland, S. E., Coxon, J., Pedatella, N. M., ... Reistad, J. P. (2017, Mar 01). North-South asymmetries in Earth's magnetic field. *Space Science Reviews*, *206*(1), 225–257. Retrieved from https://doi.org/10.1007/s11214-016-0273-0 doi: 10.1007/s11214-016-0273-0

Laundal, K. M., Finlay, C. C., & Olsen, N. (2016, Aug 11). Sunlight effects on the 3D polar current system determined from low Earth orbit measurements. *Earth, Planets and Space*, *68*(1), 142. Retrieved from https://doi.org/10.1186/s40623-016-0518-x doi: 10.1186/s40623-016-0518-x

Laundal, K. M., & Østgaard, N. (2009, 07 23). Asymmetric auroral intensities in the Earth's Northern and Southern hemispheres. *Nature*, *460*, 491 EP -. Retrieved from http://dx.doi.org/10.1038/nature08154

Milan, S. E., Clausen, L. B. N., Coxon, J. C., Carter, J. A., Walach, M.-T., Laundal, K., ... Anderson, B. J. (2017, Mar 01). Overview of solar wind–magnetosphere–ionosphere–atmosphere coupling and the generation of magnetospheric currents. *Space Science Reviews*, *206*(1), 547–573. Retrieved from https://doi.org/10.1007/s11214-017-0333-0 doi: 10.1007/s11214-017-0333-0

Newell, P. T., Meng, C.-I., & Lyons, K. M. (1996). Suppression of discrete aurorae by sunlight. *Nature*, *381*(6585), 766–767. Retrieved from https://doi.org/10.1038/381766a0 doi: 10.1038/381766a0

Ohtani, S., Ueno, G., & Higuchi, T. (2005). Comparison of large-scale field-aligned currents under sunlit and dark ionospheric conditions. *Journal of Geophysical Research: Space Physics*, *110*(A9). Retrieved from https://agupubs.onlinelibrary.wiley.com/doi/abs/10.1029/2005JA011057 doi: 10.1029/2005JA011057

Østgaard, N., & Laundal, K. M. (2013). Auroral asymmetries in the conjugate hemispheres and interhemispheric currents. In *Auroral phenomenology and magne-*

tospheric processes: Earth and other planets (p. 99-112). American Geophysical Union (AGU). Retrieved from https://agupubs.onlinelibrary.wiley.com/doi/abs/10.1029/2011GM001190 doi: 10.1029/2011GM001190

Østgaard, N., Reistad, J. P., Tenfjord, P., Laundal, K. M., Snekvik, K., Milan, S., & Haaland, S. (2015). Mechanisms that produce auroral asymmetries in conjugate hemispheres. In *Auroral dynamics and space weather* (p. 131-143). American Geophysical Union (AGU). Retrieved from https://agupubs.onlinelibrary.wiley.com/doi/abs/10.1002/9781118978719.ch10 doi: 10.1002/9781118978719.ch10

Papitashvili, V. O., Christiansen, F., & Neubert, T. (2002). A new model of field-aligned currents derived from high-precision satellite magnetic field data. *Geophysical Research Letters*, *29*(14), 28-1–28-4. Retrieved from http://dx.doi.org/10.1029/2001GL014207 doi: 10.1029/2001GL014207

Pettigrew, E. D., Shepherd, S. G., & Ruohoniemi, J. M. (2010). Climatological patterns of high-latitude convection in the northern and southern hemispheres: Dipole tilt dependencies and interhemispheric comparisons. *Journal of Geophysical Research: Space Physics*, *115*(A7). Retrieved from https://agupubs.onlinelibrary.wiley.com/doi/abs/10.1029/2009JA014956 doi: 10.1029/2009JA014956

Picone, J. M., Hedin, A. E., Drob, D. P., & Aikin, A. C. (2002). NRLMSISE-00 empirical model of the atmosphere: Statistical comparisons and scientific issues. *Journal of Geophysical Research: Space Physics*, *107*(A12), SIA 15-1–SIA 15-16. Retrieved from http://dx.doi.org/10.1029/2002JA009430 (1468) doi: 10.1029/2002JA009430

Schunk, R. W., & Nagy, A. F. (2009). *Ionospheres: Physics, plasma physics, and chemistry*. Cambridge, UK: Cambridge University Press.

Sheng, C., Deng, Y., Yue, X., & Huang, Y. (2014). Height-integrated pedersen conductivity in both e and f regions from cosmic observations. *Journal of Atmospheric and Solar-Terrestrial Physics*, *115-116*, 79 - 86. Retrieved from http://www.sciencedirect.com/science/article/pii/S1364682613003313 (Sun-Earth System Exploration: Moderate and Extreme Disturbances) doi: https://doi.org/10.1016/j.jastp.2013.12.013

Shepherd, S. G. (2014). Altitude-adjusted corrected geomagnetic coordinates: Definition and functional approximations. *Journal of Geophysical Research: Space Physics*, *119*(9), 7501–7521. Retrieved from http://dx.doi.org/10.1002/2014JA020264 doi: 10.1002/2014JA020264

Smith, A. R. A., Beggan, C. D., Macmillan, S., & Whaler, K. A. (2017). Climatology of the auroral electrojets derived from the along-track gradient of magnetic field intensity measured by pogo, magsat, champ, and swarm. *Space Weather*, *15*(10), 1257-1269. Retrieved from https://agupubs.onlinelibrary.wiley.com/doi/abs/10.1002/2017SW001675 doi: 10.1002/2017SW001675

Vanhamäki, H., & Juusola, L. (2020). Introduction to spherical elementary current systems. In M. W. Dunlop & H. Lühr (Eds.), *Ionospheric multi-spacecraft analysis tools: Approaches for deriving ionospheric parameters* (pp. 5–33). Cham: Springer International Publishing. Retrieved from https://doi.org/10.1007/978-3-030-26732-2_2 doi: 10.1007/978-3-030-26732-2_2

Vanhamäki, H., Juusola, L., Kauristie, K., Workayehu, A., & Käki, S. (2020). Spherical elementary current systems applied to swarm data. In M. W. Dunlop & H. Lühr (Eds.), *Ionospheric multi-spacecraft analysis tools: Approaches for deriving ionospheric parameters* (pp. 35–53). Cham: Springer International Publishing. Retrieved from https://doi.org/10.1007/978-3-030-26732-2_3 doi: 10.1007/978-3-030-26732-2_3

Workayehu, A. B., Vanhamki, H., & Aikio, A. T. (2019). Field-aligned and horizontal currents in the northern and southern hemispheres from the swarm

satellite. *Journal of Geophysical Research: Space Physics*, *124*(0). Retrieved from https://agupubs.onlinelibrary.wiley.com/doi/abs/10.1029/2019JA026835 doi: 10.1029/2019JA026835